

# Semi-analytical calculation of the trajectory of relativistic nuclear collisions in the QCD phase diagram

Todd Mendenhall\* and Zi-Wei Lin†

*Department of Physics, East Carolina University, Greenville, NC 27858*

(Dated: November 30, 2021)

## Abstract

We extend a semi-analytical model that includes the finite nuclear thickness to calculate the energy density  $\epsilon(t)$  and conserved-charge densities including the net-baryon density  $n_B(t)$  produced at mid-pseudorapidity in central Au+Au collisions at different energies. Assuming the formation of an equilibrated quark-gluon plasma with either quantum statistics or Boltzmann statistics, we extract the temperature  $T$  and chemical potentials  $\mu_B, \mu_S$  and  $\mu_Q$  as functions of time. This then allows us to semi-analytically calculate the  $T - \mu_B$  trajectory of relativistic nuclear collisions in the QCD phase diagram, which should benefit the studies of high density physics including the search for the critical end point. This model is also useful for exploring the trajectories in the more general QCD phase diagram in the  $T - \mu_B - \mu_S - \mu_Q$  space.

---

\*Electronic address: [mendenhallt16@students.ecu.edu](mailto:mendenhallt16@students.ecu.edu)

†Electronic address: [linz@ecu.edu](mailto:linz@ecu.edu)

## I. INTRODUCTION

Experiments at the Relativistic Heavy Ion Collider (RHIC) at BNL [1] and the Large Hadron Collider (LHC) at CERN [2] have produced the Quark-Gluon Plasma (QGP) with ultrarelativistic nuclear collisions. The QGP is an exotic phase of matter in which the temperature and density are high enough to “melt” hadrons [3]. Such a system of unbound quarks and gluons can only exist for a short time before the partons recombine into hadrons due to confinement. The fleeting nature of the QGP makes studying its properties very difficult, but the success in this endeavor would expand our understanding of the earliest stage of the universe during which the QGP is believed to have existed. Learning about the QGP properties would also enable the testing of Quantum ChromoDynamics (QCD) as the fundamental physical theory governing the strong interaction [4]. Of particular interest to the field is understanding the phase transition from hadronic to partonic matter in the QCD phase diagram [5]. Lattice QCD results show that it is a smooth crossover at zero baryon chemical potential  $\mu_B$  [6], but calculations at finite  $\mu_B$  are difficult [7].

The conjectured critical end point (CEP) of the first-order phase transition line is of special interest [8]. The Beam Energy Scan (BES) program at RHIC uses Au+Au collisions at a variety of energies to search for the CEP [9–11]. The matter created in a given collision system at a given energy follows a unique trajectory and freezes out at a given point in the QCD phase diagram on average (i.e., after averaging over many events), where temperature  $T$  and baryon chemical potential  $\mu_B$  together determine the system’s history in the QCD phase diagram. For those collisions where the freezeout point is near the CEP, event-by-event fluctuations in conserved quantities could point to the existence of the CEP [12]. For example, event-by-event net-proton cumulant fluctuations at low collision energies could prove useful for locating the CEP [13].

Since the matter in ultrarelativistic nuclear collisions progresses through several stages, it is not straightforward to correlate experimental measurements with the QGP thermodynamic properties. Dynamical models including hydrodynamic models and transport models [14–17] have been used to study the evolution of the thermodynamic properties of the QCD matter created during high energy nuclear collisions. Additionally, semi-analytical models of the initial energy density production [18–20] have progressively expanded our understanding of the early time evolution of the energy densities produced in such collisions. In

particular, it has been shown that the effect of the finite nuclear thickness drastically alters the peak energy density  $\epsilon^{max}$  at low collision energies such as the BES energies [19, 20].

The purpose of this study is to calculate trajectories in the QCD phase diagram of the matter produced in central Au+Au collisions for collision energies  $\sqrt{s_{NN}}$  up to 200 GeV. Note that all of our results here are for the central pseudorapidity region ( $\eta = 0$ ), where our semi-analytical model [20] has been defined. The paper is organized into the following sections after the Introduction. First, we describe our semi-analytical model [20] for calculating  $\epsilon(t)$  and conserved-charge densities including  $n_B(t)$  in Sec. II A. Second, we discuss the thermodynamic equations governing a massless QGP under Bose-Einstein (BE) and Fermi-Dirac (FD) statistics in Sec. II B and Boltzmann statistics in Sec. II C. For the remainder of this paper, we will refer to BE and FD statistics together as quantum statistics. For completeness, the general relations between  $\epsilon, n$  and  $T, \mu$  that lead to the thermodynamic equations of our semi-analytical model are given in the Appendix, including those for quantum statistics and Boltzmann statistics. Third, we present our results for  $\epsilon(t)$  and  $n_B(t)$  in Sec. III A, and then give our results for the extracted  $T(t), \mu_B(t), \mu_S(t), \mu_Q(t)$  and the resultant  $T - \mu_B$  trajectories for a massless QGP under quantum statistics in Sec. III B and Boltzmann statistics in Sec. III C. We also present our results for the QGP lifetime in Sec. III D. Then, we discuss the effect of a finite  $s$ -quark mass and interesting details regarding the near-zero value of the calculated  $\mu_Q$  in Sec. IV. Finally, we conclude in Sec. V.

## II. METHODS

### A. Calculating energy and net-charge densities

Naively, one can use the method of the Bjorken energy density formula [18], in which partons at mid-pseudorapidity are produced at  $t = 0$  and  $z = 0$ , to predict the time evolution of the initial energy density  $\epsilon(t)$ :

$$\epsilon^{Bj}(t) = \frac{1}{tA_T} \frac{dE_T}{dy}. \quad (1)$$

Here,  $A_T = \pi R_A^2$  is the transverse overlap area of two nuclei in central collisions, and  $dE_T/dy$  is the transverse energy density at mid-rapidity. Because Eq.(1) predicts a diverging  $\epsilon$  as  $t \rightarrow 0$ , one must choose a finite initial time  $\tau_F$ , which can be considered as the time when

partons are formed. For high collision energies, such as the top RHIC energy of  $\sqrt{s_{\text{NN}}} = 200$  GeV, the finite thickness of the Lorentz-contracted nucleus is small compared to the typical  $\tau_F$  value, so Bjorken's formula is valid. However, at lower energies where the crossing time  $d_t = 2R_A/\sinh y_{CM}$  is comparable to or even greater than  $\tau_F$ , Eq.(1) is expected to break down [21]. Note that we use  $R_A = 1.12A^{1/3}$  fm for the hard-sphere nuclear radius and  $y_{CM}$  as the rapidity of the projectile nucleus in the center-of-mass frame. Also note that the transverse expansion of the overlap volume, the slowing down of participant nucleons, and secondary parton or hadron scatterings are neglected in our semi-analytical study, as done in previous similar studies [18–20].

We have shown earlier [19, 20] that the finite nuclear thickness must be considered when estimating  $\epsilon(t)$  at low collision energies. Thus, a more realistic model of the initial energy production is one in which partons are produced within a finite range of time and longitudinal position [20]. This improved model has been shown to predict a finite  $\epsilon^{max}$  for  $\tau_F = 0$  fm/c, while earlier models [18, 19] predict infinite  $\epsilon^{max}$  there. In this model [20], the initial energy density at time  $t$  averaged over the full transverse overlap area is given by

$$\epsilon(t) = \frac{1}{A_T} \iint_S \frac{dx dz_0}{t-x} \frac{d^3 m_T}{dx dz_0 dy} \cosh^3 y \quad (2)$$

In the above,  $S$  represents the production area in the initial production time  $x$  and longitudinal position  $z_0$  at observation time  $t$ . To be general, the initial energy is assumed to be produced within  $x \in [t_1, t_2]$  (instead of the naive range  $[0, d_t]$ ). The resulting  $\epsilon(t)$  is a piecewise function of  $t$ , where the pieces are determined by the integration limits in Eq.(2) and are listed in Table I (see Ref. [20] for details). Note that  $\epsilon(t) = 0$  when  $t \in [0, t_1 + \tau_F)$ .

In this study, we assume that  $d^3 m_T/(dx dz_0 dy)$  in Eq.(2) can be factored:

$$\frac{d^3 m_T}{dx dz_0 dy} = g(z_0, x) \frac{dm_T}{dy}. \quad (3)$$

The weighting function  $g(z_0, x)$  is normalized as  $\iint_{S_0} g(z_0, x) dx dz_0 = 1$ , where  $S_0$  is the entire production diamond area in the  $t-z$  plane [20]. This normalization condition ensures that  $dm_T/dy$  represents the initial transverse mass rapidity density of all produced partons. We further make the simplest assumption that partons are produced uniformly throughout the entire production area  $S_0$ , which leads to  $g(z_0, x) = 2/(\beta t_{21}^2)$ , where  $\beta = \tanh y_{CM}$  and  $t_{21} = t_2 - t_1$ . Next, we take the following specific form for  $dm_T/dy$  [20]:

$$\frac{dm_T}{dy} = \frac{dE_T}{dy} + m_N \frac{dN_B}{dy}. \quad (4)$$

Piece	$t$ -range	$x$ -range	$z_0$ -range
$\epsilon_I(t)$ or $n_{B,I}(t)$	$[t_1 + \tau_F, t_a)$	$[t_1, x_1)$ $[x_1, t - \tau_F]$	$[-\beta(x - t_1), \beta(x - t_1)]$ $[-z_F(x), z_F(x)]$
$\epsilon_{II}(t)$ or $n_{B,II}(t)$	$[t_a, t_2 + \tau_F)$	$[t_1, t_{mid})$ $[t_{mid}, x_2)$ $[x_2, t - \tau_F]$	$[-\beta(x - t_1), \beta(x - t_1)]$ $[-\beta(t_2 - x), \beta(t_2 - x)]$ $[-z_F(x), z_F(x)]$
$\epsilon_{III}(t)$ or $n_{B,III}(t)$	$[t_2 + \tau_F, \infty)$	$[t_1, t_{mid})$ $[t_{mid}, x_2]$	$[-\beta(x - t_1), \beta(x - t_1)]$ $[-\beta(t_2 - x), \beta(t_2 - x)]$

TABLE I: Piecewise solution of  $\epsilon(t)$  and  $n_B(t)$  as functions of the observation time  $t$ , where the integration limits for each piece are written in the format  $x \in [x_{min}, x_{max}]$  and  $z_0 \in [z_0^{min}, z_0^{max}]$  for each part of the production area in the initial production time  $x$  and longitudinal position  $z_0$  [20].

We assume that the  $dE_T/dy$  term is described by a single Gaussian function of rapidity while  $dN_B/dy$  is described by a double Gaussian function of rapidity [20]:

$$\frac{dE_T}{dy} = \frac{dE_T}{dy}(0) \exp\left(-\frac{y^2}{2\sigma^2}\right), \quad (5)$$

$$\frac{dN_B}{dy} = C \left[ \exp\left(-\frac{(y + y_B)^2}{2\sigma_B^2}\right) + \exp\left(-\frac{(y - y_B)^2}{2\sigma_B^2}\right) \right]. \quad (6)$$

The transverse energy rapidity density at mid-rapidity is parameterized as  $dE_T/dy(0) = 1.25dE_T/d\eta(0)$ , where  $dE_T/d\eta(0)$  at  $\sqrt{s_{NN}} > 20.7$  GeV is taken as the parameterization given by the PHENIX Collaboration [22], while  $dE_T/d\eta(0)$  at lower energies is given by the following improved parameterization [20]:

$$\frac{dE_T}{d\eta}(0) = 0.308N_p \ln^{1.08}\left(\frac{\sqrt{s_{NN}}}{E_0}\right) \quad (7)$$

with  $E_0 = 2m_N$  being the threshold energy. We take the number of participants to be  $N_p = 2A$  for central A+A collisions that we consider in this study. We also use the following parameterizations for the Gaussian parameters  $y_B$  and  $\sigma_B$  [20]:

$$y_B = 0.541 \left(\frac{\sqrt{s_{NN}} - E_0}{\text{GeV}}\right)^{0.196} \ln^{0.392}\left(\frac{\sqrt{s_{NN}}}{E_0}\right), \quad (8)$$

$$\sigma_B = 0.601 \left(\frac{\sqrt{s_{NN}} - E_0}{\text{GeV}}\right)^{0.121} \ln^{0.241}\left(\frac{\sqrt{s_{NN}}}{E_0}\right). \quad (9)$$

These parameterizations have been obtained using the proton  $dN/dy$  data at  $\sqrt{s_{NN}} = 2.4, 3.1, 3.6,$  and  $4.1$  GeV [23] and the net-proton  $dN/dy$  data at  $\sqrt{s_{NN}} = 5$  [24],  $17.3$  [25], and

200 GeV [26] in central Au+Au collisions (with the exception that central Pb+Pb data are used at 17.3 GeV). The value of  $C$  in Eq.(6) is determined from the conservation of total net-baryon number  $\int (dN_B/dy)dy = 2A$  at each collision energy. Finally, the Gaussian parameter  $\sigma$  in Eq.(5) is calculated using the conservation of total energy  $\int (dm_T/dy) \cosh y dy = A\sqrt{s_{NN}}$  at each collision energy.

In our semi-analytical model [19, 20], the primary collisions between the two nuclei start at time  $t_1$  and end at time  $t_2$ . In this study, we take

$$t_1 = \frac{1}{6}d_t, \quad t_2 = \frac{5}{6}d_t, \quad (10)$$

because this choice gives  $\epsilon^{max} = 2\rho_0 m_N$  and  $n_B^{max} = 2\rho_0$  for the threshold collision energy  $\sqrt{s_{NN}} = 2m_N$ , which would be expected if the two nuclei would just fully overlap. Note that  $\rho_0 \approx 0.17 \text{ fm}^{-3}$  in the hard sphere model for the nucleus. Also note that in previous studies [19, 20],  $t_1 = 0.2d_t$  and  $t_2 = 0.8d_t$  were used so that the width of the production time distribution was similar to the results from the string melting version of a multi-phase transport (AMPT) model [27]. In Table I, time  $t_a$  is given by

$$t_a = \frac{t_{mid}}{2} + \sqrt{\tau_F^2 + \left(\frac{\beta t_{21}}{2}\right)^2} \quad (11)$$

with  $t_{mid} = (t_1 + t_2)/2$ , times  $x_1$  and  $x_2$  are given by

$$x_i = \frac{t - \beta^2 t_i - \sqrt{\beta^2 [(t - t_i)^2 - \tau_F^2] + \tau_F^2}}{1 - \beta^2} \quad \text{for } i = 1, 2, \quad (12)$$

and the function  $z_F(x)$  is given by

$$z_F(x) = \sqrt{(t - x)^2 - \tau_F^2}. \quad (13)$$

In this study, we calculate the net-charge densities such as the net-baryon density  $n_B(t)$  using the same method as that used for the  $\epsilon(t)$  calculation [20]. We then obtain the following equation for the net-baryon density similar to Eq.(2):

$$n_B(t) = \frac{1}{A_T} \iint_S \frac{dx dz_0}{t - x} \frac{d^3 N_B}{dx dz_0 dy} \cosh^2 y. \quad (14)$$

Note that there is one less power of  $\cosh y$  in this equation than in Eq.(2) because that equation involves  $E = m_T \cosh y$ . We also use the same  $dN_B/dy$  parameterization [20] as shown in Eq.(6) and assume the same factorization  $d^3 N_B/(dx dz_0 dy) = 2/(\beta t_{21}^2) dN_B/dy$ .

Therefore, the net-baryon density  $n_B(t)$  is also given by a piecewise solution, as shown in Table I.

Since the net-electric charge is carried by the incoming protons while the net-baryon number is carried by the incoming nucleons in the nuclei, we assume that the initial production from the primary NN collisions is independent of whether N is a proton or a neutron. Our semi-analytical method then leads to

$$n_Q(t) = \frac{Z}{A}n_B(t), \quad (15)$$

where  $Z$  and  $A$  represent the atomic number and mass number of the nucleus, respectively, in the symmetric collisional system. Note that the relationship  $n_Q/n_B = Z/A$  has also been used in other studies [28]. Furthermore, since the incoming nuclei do not carry net-strangeness, we assume that the initial production is symmetric for  $s$  and  $\bar{s}$ , our semi-analytical method then simply gives

$$n_S(t) = 0 \quad (16)$$

for the net-strangeness density.

## B. Thermodynamics of a massless QGP under quantum statistics

According to Eq.(A.9) or Eq.(A.13), the result  $n_S = 0$  from our semi-analytical model gives the following relation

$$\mu_B - \mu_Q - 3\mu_S = 0 \quad (17)$$

for both quantum or Boltzmann statistics, which also corresponds to  $\mu_s = 0$  for the strange quark chemical potential. Using this relation, the general results in Eqs.(A.6)-(A.8) for quantum statistics simplify to the following set of equations:

$$\epsilon = \frac{19\pi^2}{12}T^4 + 3\frac{(\mu_B - 2\mu_S)^2 + \mu_S^2}{2}T^2 + 3\frac{(\mu_B - 2\mu_S)^4 + \mu_S^4}{4\pi^2}, \quad (18)$$

$$n_B = \frac{\mu_B - \mu_S}{3}T^2 + \frac{(\mu_B - 2\mu_S)^3 + \mu_S^3}{3\pi^2}, \quad (19)$$

$$n_Q = \frac{2\mu_B - 5\mu_S}{3}T^2 + \frac{2(\mu_B - 2\mu_S)^3 - \mu_S^3}{3\pi^2}. \quad (20)$$

We refer to the  $T$ ,  $\mu_B$ ,  $\mu_S$  and  $\mu_Q$  values extracted from the  $\epsilon$ ,  $n_B$ , and  $n_Q$  values using Eqs.(17)-(20) as the “full solution” for quantum statistics.

On the other hand, if we ignore the electric charge by setting  $\mu_Q = 0$ , Eq.(17) gives  $\mu_S = \mu_B/3$ , which leads to the following simplified equations:

$$\epsilon_1 = \frac{19\pi^2}{12}T^4 + \frac{\mu_B^2}{3}T^2 + \frac{\mu_B^4}{54\pi^2}, \quad (21)$$

$$n_{B,1} = \frac{2\mu_B}{9}T^2 + \frac{2\mu_B^3}{81\pi^2}. \quad (22)$$

We refer to the  $T$ ,  $\mu_B$  (and  $\mu_S$ ,  $\mu_Q$ ) values extracted from the  $\epsilon$  and  $n_B$  values using Eqs.(21)-(22) as the ‘‘partial-1 solution’’ for quantum statistics. However, note that in this case Eq.(20) would give  $n_Q = n_B/2$ , which is inconsistent with the result  $n_Q = Zn_B/A$  from our semi-analytical model. This discrepancy, which also exists for the Boltzmann statistics, is a consequence of the partial solution not being the full solution.

Additionally, if one ignores both the electric charge and strangeness by setting  $\mu_Q = \mu_S = 0$ , Eqs.(A.6)-(A.7) lead to the following different set of simplified equations:

$$\epsilon_2 = \frac{19\pi^2}{12}T^4 + \frac{\mu_B^2}{2}T^2 + \frac{\mu_B^4}{36\pi^2}, \quad (23)$$

$$n_{B,2} = \frac{\mu_B}{3}T^2 + \frac{\mu_B^3}{27\pi^2}. \quad (24)$$

We refer to the  $T$ ,  $\mu$  values extracted from the  $\epsilon$  and  $n_B$  values using Eqs.(23)-(24) as the ‘‘partial-2 solution’’ for quantum statistics. Note that this approximation is inconsistent with Eq.(17) from our semi-analytical model. In addition, in this case Eqs.(A.8)-(A.9) would give  $n_Q = 0$  and  $n_S = -n_B$  (same for the Boltzmann statistics), which are more inconsistent with the results from our semi-analytical model [20] or the numerical results from the AMPT model study [17].

### C. Thermodynamics of a massless QGP under Boltzmann statistics

Using Eq.(17) that is also valid for Boltzmann statistics, the general results in Eqs.(A.10)-(A.13) simplify to the following set of equations:

$$\epsilon = \frac{12}{\pi^2}T^4 \left[ 7 + 3 \cosh \left( \frac{\mu_B - 2\mu_S}{T} \right) + 3 \cosh \left( \frac{\mu_S}{T} \right) \right], \quad (25)$$

$$n_B = \frac{4}{\pi^2}T^3 \left[ \sinh \left( \frac{\mu_B - 2\mu_S}{T} \right) + \sinh \left( \frac{\mu_S}{T} \right) \right], \quad (26)$$

$$n_Q = \frac{4}{\pi^2}T^3 \left[ 2 \sinh \left( \frac{\mu_B - 2\mu_S}{T} \right) - \sinh \left( \frac{\mu_S}{T} \right) \right]. \quad (27)$$



They provide the full solution of  $T$  and  $\mu$  for Boltzmann statistics.

Again, if we ignore electric charge by setting  $\mu_Q = 0$ , we then have  $\mu_S = \mu_B/3$ , which leads to the following simplified equations that determine the partial-1 solution for Boltzmann statistics:

$$\epsilon_1 = \frac{12}{\pi^2} T^4 \left[ 7 + 6 \cosh \left( \frac{\mu_B}{3T} \right) \right], \quad (28)$$

$$n_{B,1} = \frac{8}{\pi^2} T^3 \sinh \left( \frac{\mu_B}{3T} \right). \quad (29)$$

Alternatively, if one sets  $\mu_Q = \mu_S = 0$ , one would simplify Eqs.(A.10)-(A.11) to the following equations that determine the partial-2 solution for Boltzmann statistics:

$$\epsilon_2 = \frac{12}{\pi^2} T^4 \left[ 4 + 9 \cosh \left( \frac{\mu_B}{3T} \right) \right], \quad (30)$$

$$n_{B,2} = \frac{12}{\pi^2} T^3 \sinh \left( \frac{\mu_B}{3T} \right). \quad (31)$$

### III. RESULTS

#### A. Energy and net-baryon density

Figure 1 shows the results of  $\epsilon(t)$  and  $n_B(t)$  at mid-rapidity averaged over the transverse overlap area for central Au+Au collisions at three different energies. The results from our semi-analytical model at  $\tau_F = 0.1$  (solid) and 0.3 fm/c (dashed) are shown together with the results from the Bjorken model at  $\tau_F = 0.1$  fm/c (dot-dashed). We see that the peak energy density  $\epsilon^{max}$  from our model increases as  $\sqrt{s_{NN}}$  increases, while the peak net-baryon density  $n_B^{max}$  may first increase from low to mid  $\sqrt{s_{NN}}$  and then decrease with  $\sqrt{s_{NN}}$ .

We also see the large effect that the finite nuclear thickness has on the predicted densities at low energies [19, 20]. Compared to the results from the Bjorken model [18], our results from Eq.(2) and Eq.(14) have significantly smaller  $\epsilon^{max}$  and  $n_B^{max}$  at lower collision energies, while the difference decreases and eventually vanishes at high collision energies as expected. Therefore, we expect significant differences in the  $T - \mu_B$  trajectories at low energies between our results and the results from the Bjorken model. Note that the net-baryon density in the Bjorken model is given by

$$n_B^{Bj}(t) = \frac{1}{tA_T} \frac{dN_B}{dy}. \quad (32)$$

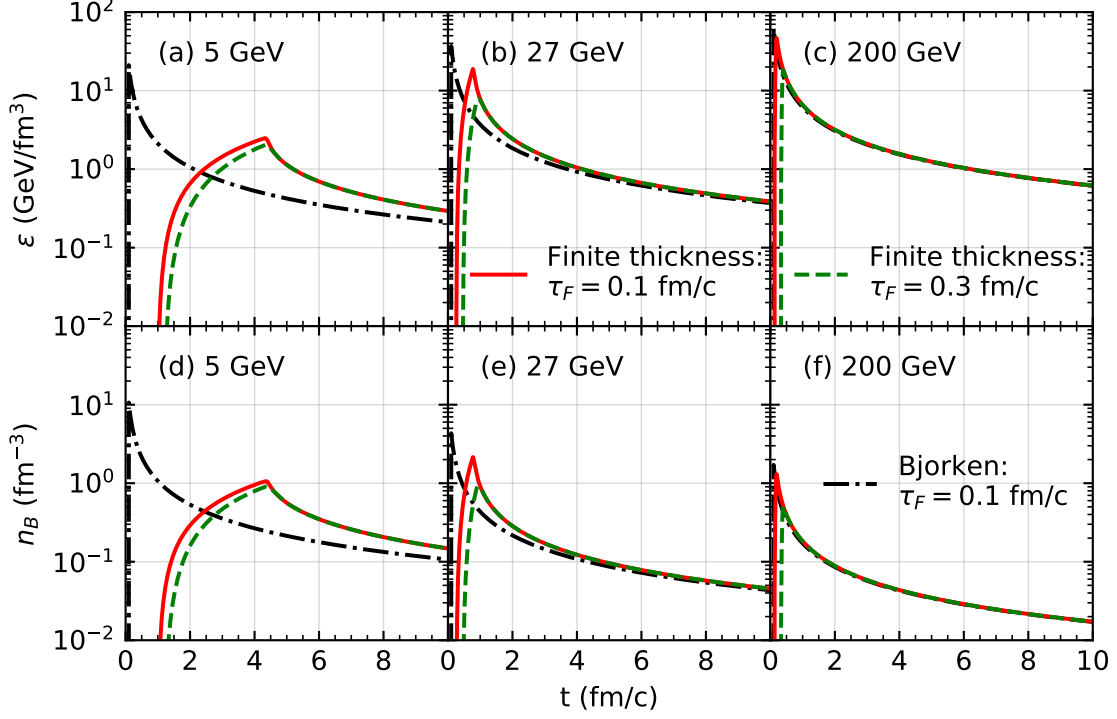


FIG. 1:  $\epsilon(t)$  (upper panels) and  $n_B(t)$  (lower panels) at mid-rapidity averaged over the transverse area for central Au+Au collisions at  $\sqrt{s_{NN}} = 5, 27$  and  $200$  GeV from our model for  $\tau_F = 0.1$  (solid) and  $0.3$  fm/c (dashed) in comparison with results from the Bjorken model for  $\tau_F = 0.1$  fm/c (dot-dashed).

### B. Trajectory of a massless QGP with quantum statistics

In Figure 2, we show the  $T$  and  $\mu$  results extracted from the full solution of Eqs.(18)-(20), the partial-1 solution of Eqs.(21)-(22), and the partial-2 solution of Eqs.(23)-(24). We see that the peak temperature  $T^{max}$  increases as  $\sqrt{s_{NN}}$  increases, while the peak net-baryon chemical potential  $\mu_B^{max}$  decreases as  $\sqrt{s_{NN}}$  increases (from 5 GeV) for all three solutions. It is also obvious that both  $T$  and  $\mu_B$  reach the peak value earlier as  $\sqrt{s_{NN}}$  increases due to the shorter duration time  $d_t$  at higher energies.

Figure 2 also shows that the partial-1 solution reproduces the  $T(t)$  and  $\mu_B(t)$  results from the full solution almost exactly over the entire time evolution. On the other hand, the partial-2 solution gives a much smaller  $\mu_B$  and a slightly larger  $T$  than the full solution at low collision energies. We see that the magnitude of  $\mu_Q$  in the full solution is very small ( $\lesssim 30$  MeV), so the assumption  $\mu_Q = 0$  in both the partial-1 and partial-2 solutions seems

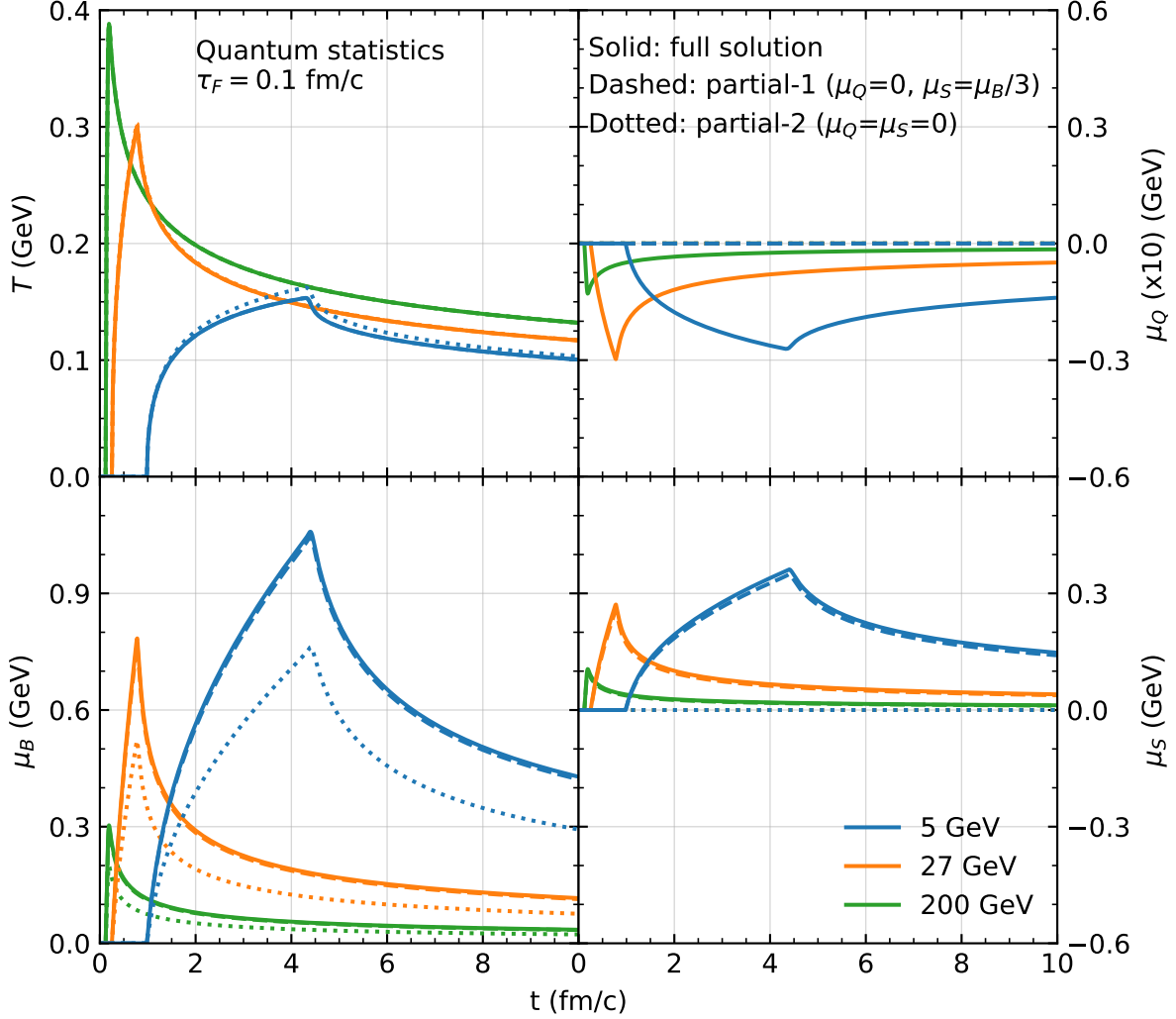


FIG. 2:  $T(t)$ ,  $\mu_B(t)$ ,  $\mu_Q(t)$  (multiplied by a factor of 10), and  $\mu_S(t)$  for a QGP with quantum statistics from the full (solid), partial-1 (dashed), and partial-2 (dotted) solutions at  $\tau_F = 0.1$  fm/c for central Au+Au collisions at  $\sqrt{s_{NN}} = 5$  (blue), 27 (orange), and 200 (green) GeV.

reasonable. On the other hand,  $\mu_S \simeq \mu_B/3$  in the full solution indicates that the partial-1 solution that assumes  $\mu_S = \mu_B/3$  is a significant improvement over the partial-2 solution that assumes  $\mu_S = 0$ . We note that the recent numerical results from the AMPT model [17] also show  $\mu_Q \approx 0$  and  $\mu_S \approx \mu_B/3$ .

Figure 3 shows the  $T - \mu_B$  trajectories in the QCD phase diagram for quantum statistics and  $\tau_F = 0.1$  fm/c. At early times  $t \in [0, t_1 + \tau_F)$ , the system is at  $(\mu_B, T) = (0, 0)$ ; the trajectory then starts to rise. For  $\sqrt{s_{NN}} \gtrsim 4$  GeV, the trajectories pass through the crossover curve (dotted), which comes from calculations using the functional renormalization group

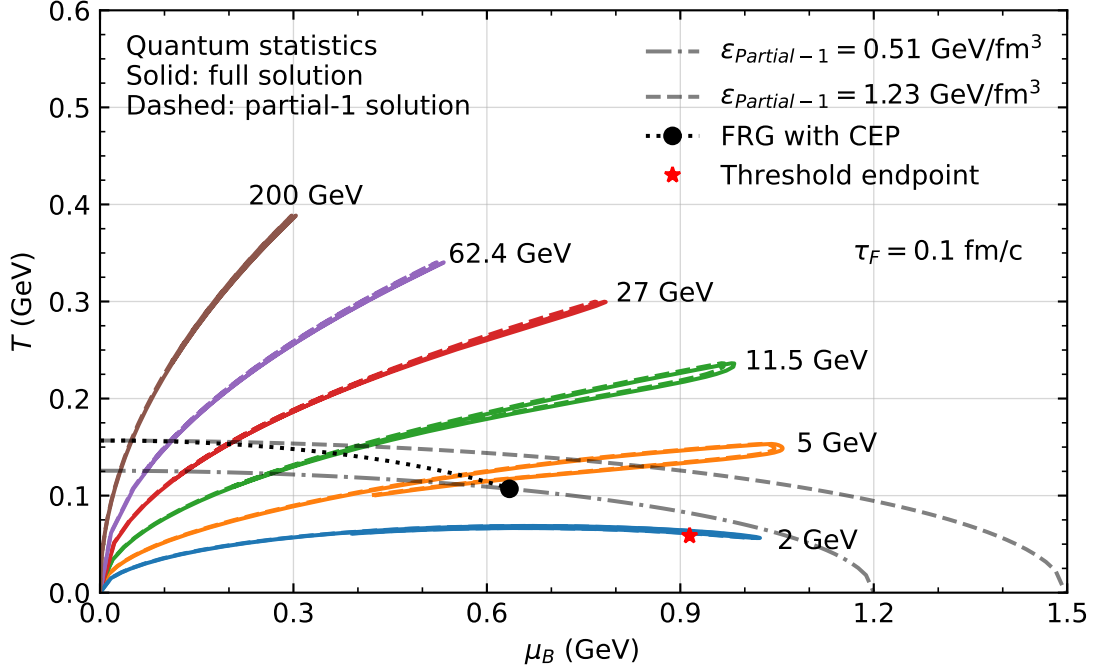


FIG. 3: Trajectories from the full (solid) and partial-1 (dashed) solutions for quantum statistics and  $\tau_F = 0.1$  fm/ $c$  for central Au+Au collisions at  $\sqrt{s_{NN}} = 2, 5, 11.5, 27, 62.4,$  and  $200$  GeV. Two constant energy density lines from the partial-1 solution, the FRG crossover curve (dotted) with CEP (circle), and the endpoint at threshold energy (star) are also shown for reference.

(FRG) with  $N_F = 2 + 1$  [29]. When a trajectory reaches the endpoint, which corresponds to the time when both  $\epsilon^{max}$  and  $n_B^{max}$  are reached, it turns clockwise and returns toward the origin. At high or very low collision energies, the returning part of the trajectory is so close to the outgoing part that the two appear to overlap. However, for intermediate collision energies such as  $\sqrt{s_{NN}} = 5$  or  $11.5$  GeV, the two parts are distinguishable. Notably, at  $\sqrt{s_{NN}} \gtrsim 4.1$  GeV both the outgoing and returning parts of the trajectory intersect the FRG crossover curve, while at  $\sqrt{s_{NN}} \lesssim 3.6$  GeV neither part of the trajectory intersects the FRG crossover curve.

We have also used Eq.(21) from the the partial-1 solution for quantum statistics to calculate the lines of constant  $\epsilon$  that goes through the two endpoints of the FRG crossover curve. They corresponds to  $\epsilon = 0.51$  (dot-dashed) and  $1.23$  (dashed) GeV/ $\text{fm}^3$ , as shown in Fig. 3. In addition, the endpoint of the trajectory at the threshold energy  $E_0$  is also calculated and shown (star), which is located at  $(\mu_B, T) \sim (0.9 \text{ GeV}, 0.06 \text{ GeV})$ .

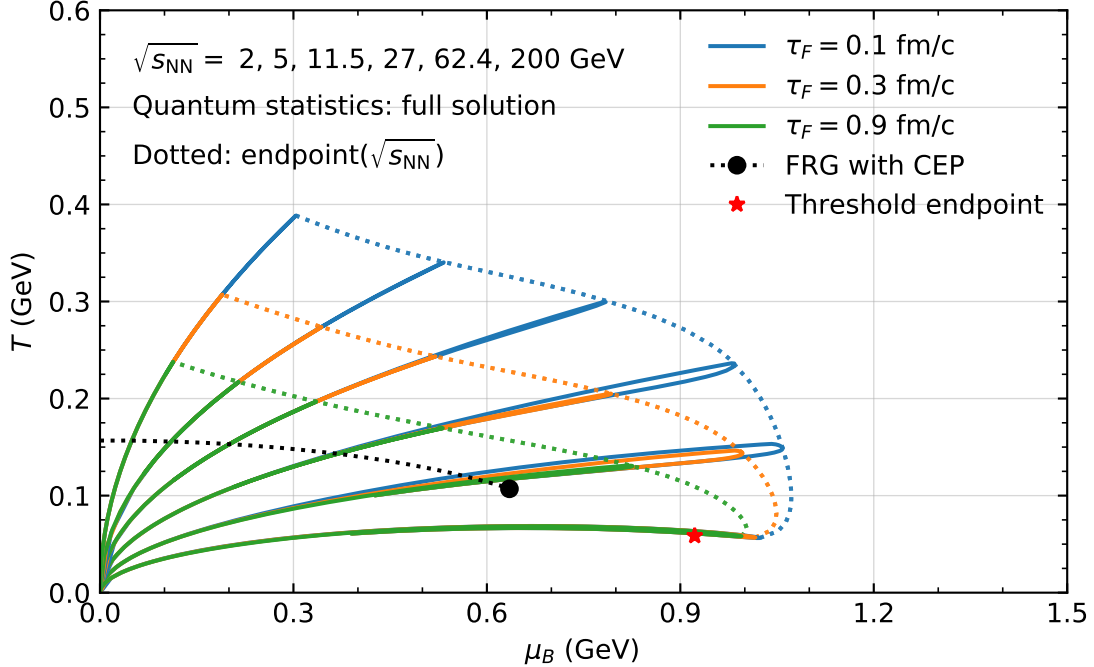


FIG. 4: Trajectories from the full solution for quantum statistics at  $\tau_F = 0.1$  (blue),  $0.3$  (orange), and  $0.9$  (green) fm/c for central Au+Au collisions at  $\sqrt{s_{\text{NN}}} = 2, 5, 11.5, 27, 62.4,$  and  $200$  GeV, together with the trajectory endpoint curves (colored dotted). The FRG crossover curve (black dotted) with CEP (circle) and the endpoint at threshold energy (star) are also shown.

The results from our semi-analytical model [20] depend on the value of  $\tau_F$ . Figure 4 shows how the  $T - \mu_B$  trajectories from the quantum statistics full solution depend on  $\tau_F$ . As  $\tau_F$  decreases, the trajectory becomes longer with the endpoint moving further to higher  $\mu_B$  (and also higher  $T$  except at very low energies). Note that the trajectory endpoint corresponds to  $\epsilon^{\text{max}}$  and  $n_B^{\text{max}}$ , but at low energies it does not necessarily correspond to  $T^{\text{max}}$  and  $\mu_B^{\text{max}}$ ; this can be seen from the 2 GeV curve in Fig. 4. We also see that the outgoing parts of the trajectories at a given energy but different  $\tau_F$  values often do not overlap well, consistent with the significant dependence of  $\epsilon(t)$  and  $n_B(t)$  on  $\tau_F$  at early times as shown in Fig. 1. On the other hand, the returning parts of the trajectories overlap well, because  $\epsilon$  and net-charge densities at late times are insensitive to  $\tau_F$ .

We have also calculated how the endpoint of a trajectory depends on the collision energy at different formation times as shown by the three colored dotted curves in Fig. 4. At high collision energies, we observe a clear separation of the endpoint curves at different  $\tau_F$  values.

At very low collision energies, however, this separation decreases and the endpoint curves at different  $\tau_F$  converge to the threshold endpoint (star). We also see that the CEP from the FRG calculation [29] at  $(\mu_B, T) = (0.635 \text{ GeV}, 0.107 \text{ GeV})$  is well within the endpoint curves (even for  $\tau_F = 0.9 \text{ fm}/c$ ), which means that this CEP location should be accessible with central Au+Au collisions. On the other hand, the  $T - \mu_B$  region below the  $\sqrt{s_{\text{NN}}} = 2 \text{ GeV}$  trajectory in the QCD phase diagram is essentially inaccessible according to our model. Note that our semi-analytical model should break down at very low energies because the initial system after the primary collisions would not be in parton degrees of freedom. However, since our model gives  $\epsilon^{\text{max}} = 2\rho_0 m_N$  and  $n_B^{\text{max}} = 2\rho_0$  at the threshold energy as one naively expects, the  $\epsilon$  and  $n_B$  values at very low energies from our model should not be far off.

### C. Trajectory of a massless QGP with Boltzmann statistics

We show in Fig. 5 the time evolutions of  $T$  and  $\mu$  extracted from the full solution of Eqs.(25)-(27), the partial-1 solution of Eqs.(28)-(29), and the partial-2 solution of Eqs.(30)-(31) for a QGP with Boltzmann statistics. Similar to the results for quantum statistics shown in Fig. 2, the full and partial-1 solutions give essentially the same results, while the partial-2 solution gives significantly smaller  $\mu_B$  (and slightly larger  $T$ ) values. In addition, the magnitudes of  $\mu_Q$  from the full solution for Boltzmann statistics are even smaller than those for quantum statistics. As a result,  $\mu_S \simeq \mu_B/3$  for the full solution here.

Figure 6 shows the  $T - \mu_B$  trajectories for  $\tau_F = 0.1 \text{ fm}/c$  from the full and partial-1 solutions. For reference, we have included the FRG crossover curve including the CEP [29]. The trajectory endpoint at the threshold energy (star) is obtained by using the partial-1 solution for Boltzmann statistics with  $\epsilon^{\text{max}} = 2\rho_0 m_N$  and  $n_B^{\text{max}} = 2\rho_0$ , and it now lies to the left of the CEP. We also show the two lines of constant  $\epsilon$  as calculated from Eq.(28) for Boltzmann statistics, which go through the endpoints of the FRG crossover curve. Interestingly, they both show a half-loop structure, which is totally different from the shape of constant- $\epsilon$  lines for quantum statistics as shown in Fig. 3. We can understand this by considering the total differential in Eq.(28):  $d\epsilon_1 = \partial_{T\epsilon_1} dT + \partial_{\mu_B\epsilon_1} d\mu_B$ . At constant energy density where  $d\epsilon_1 = 0$ , we get

$$\frac{d\mu_B}{dT} = -\frac{\partial_{T\epsilon_1}}{\partial_{\mu_B\epsilon_1}}. \quad (33)$$

The numerator in the above equation is zero when  $\mu_B/(3T) \approx 4.15$ , which corresponds to a

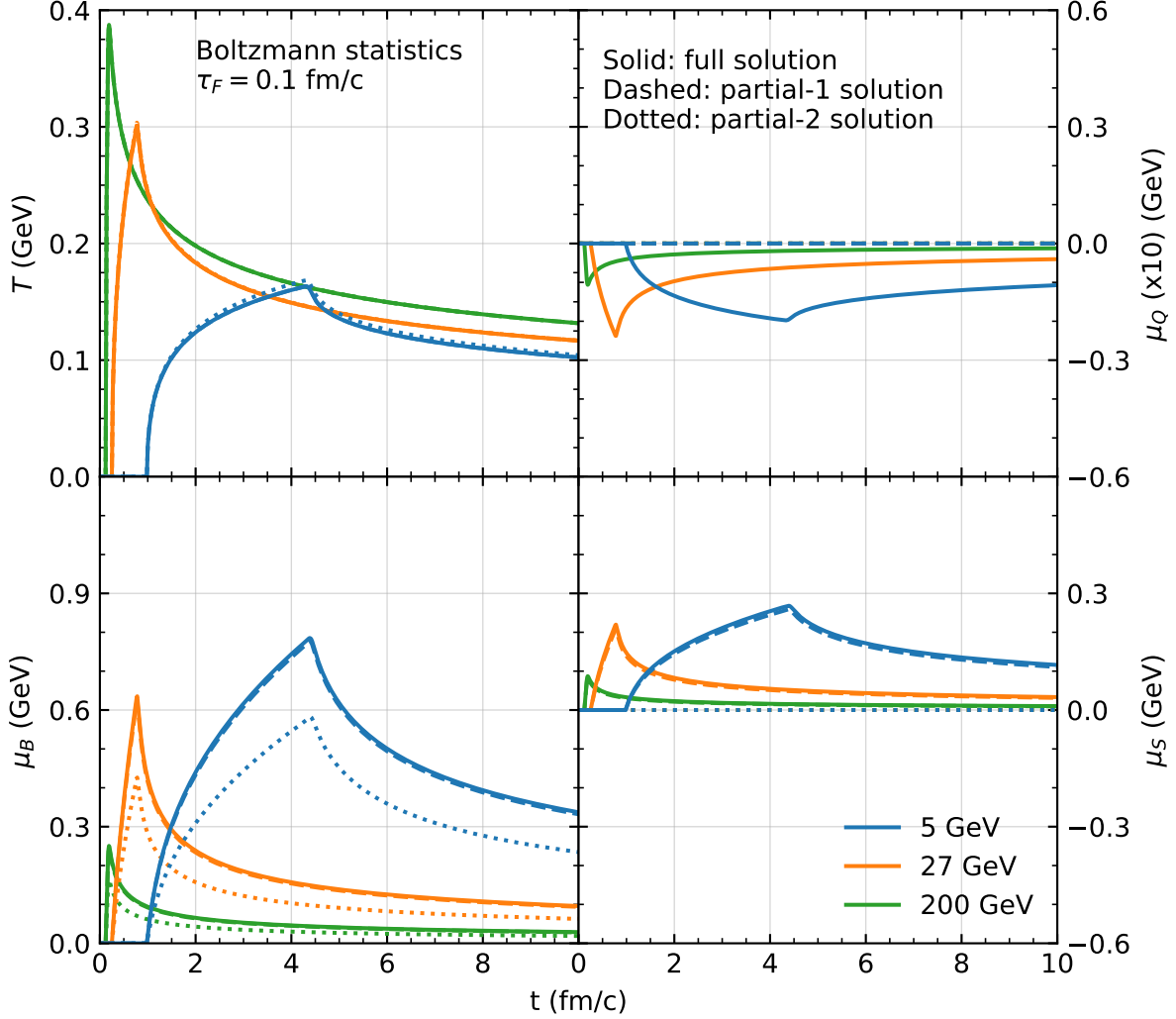


FIG. 5: Same as Fig. 2 but for Boltzmann statistics.

turning point in the line of constant energy density for Boltzmann statistics. If one follows a line of constant  $\epsilon$  starting from the higher-temperature side at  $\mu_B = 0$  (where  $\epsilon \gg n_B m_N$ ), one will arrive at a point (around the turning point) beyond which  $\epsilon < n_B m_N$ . Since it is unnatural for a nuclear matter including the QGP to have  $\epsilon < n_B m_N$  if a baryon number is effectively related to a baryon mass, the  $T - \mu_B$  points on the lower part (roughly the lower half) of each constant- $\epsilon$  curve in Fig. 6 do not represent a physical QGP system with the Boltzmann statistics.

Figure 6 also shows how the endpoint of a trajectory depends on the collision energy at different formation times. As in Fig. 4, at high collision energies we see a clear separation of the endpoint curves for different formation times. We also see the same “turning-around”

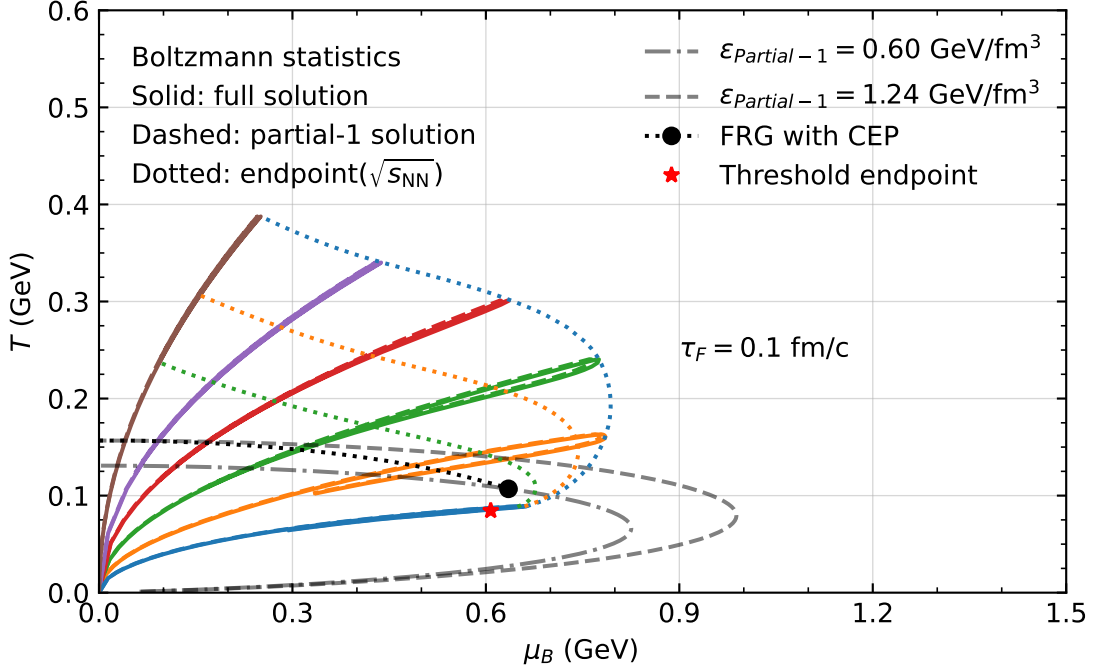


FIG. 6: Trajectories from the full (solid) and partial-1 (dashed) solutions for Boltzmann statistics and  $\tau_F = 0.1$  fm/c for central Au+Au collisions at  $\sqrt{s_{NN}} = 2, 5, 11.5, 27, 62.4,$  and  $200$  GeV together with the trajectory endpoint curves for  $\tau_F = 0.1$  (blue dotted),  $0.3$  (orange dotted), and  $0.9$  (green dotted) fm/c. Two constant energy density lines from the partial-1 solution, the FRG crossover curve (dotted) with CEP (circle), and the endpoint at threshold energy (star) are also shown.

behavior of each endpoint curve as  $\sqrt{s_{NN}}$  decreases towards the threshold energy. Notably, the CEP from the FRG calculation is now much closer to the  $\tau_F = 0.9$  fm/c endpoint curve than the case for quantum statistics. Another key difference between Figs. 6 and 4 is the location of the CEP with respect to individual trajectories. For Boltzmann statistics or Fig. 6, the CEP lies close to the returning part of the 3.1 GeV trajectory or the outgoing part of the 2.6 GeV trajectory; while for quantum statistics or Fig. 4 the CEP is close to the returning part of the 4.1 GeV trajectory or the outgoing part of the 3.6 GeV trajectory.

In Fig. 7 we compare our results with the  $T - \mu_B$  trajectories that are extracted from the  $\epsilon(t)$  and  $n_B(t)$  values calculated with the Bjorken model [18]. At high collision energies, the trajectories from the Bjorken model are rather close to our results that include the finite nuclear thickness for the same (Boltzmann) statistics, as expected. At lower collision



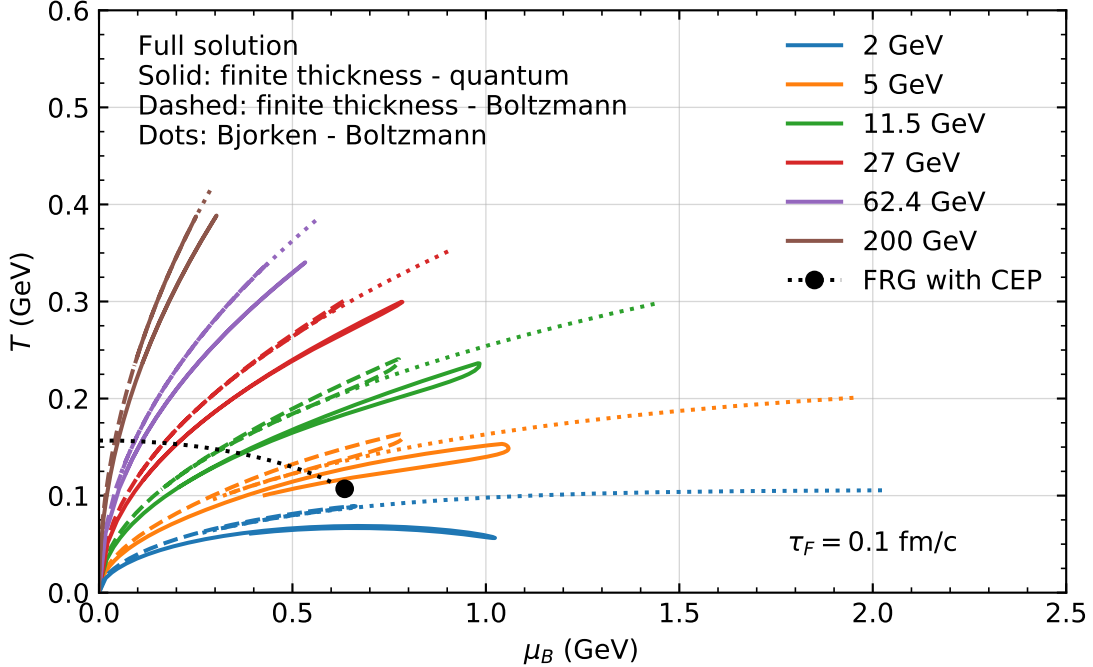


FIG. 7: Trajectories from the full solution for quantum statistics (solid) and Boltzmann statistics (dashed) extracted from our  $\epsilon(t)$  and  $n_B(t)$  in comparison with those extracted from  $\epsilon^{Bj}(t)$  and  $n_B^{Bj}(t)$  (dots) for Boltzmann statistics for central Au+Au collisions at different energies.  $\tau_F = 0.1$  fm/c for all cases, and the FRG crossover curve (black dotted) with the CEP (circle) is also shown.

energies,  $\mu_B^{max}$  from the Bjorken model is much larger, and there is no outgoing part of the trajectory since  $\epsilon^{max}$  and  $n_B^{max}$  in the Bjorken model occur at the earliest time ( $t = \tau_F$ ). In contrast, in our semi-analytical model the time of maximum density occurs much later, sometime between  $[t_a, t_2 + \tau_F]$  [20]. We also see in Fig. 7 that the late-time part of a Bjorken trajectory overlaps with the returning part of our trajectory. This is because the Bjorken model and our semi-analytical model predict the same densities for late times [19, 20], which is also shown in Fig. 1.

Comparing our results for the two statistics in Fig. 7, we see that, while the  $T^{max}$  values are often similar at the same collision energy (except at very low energies), the  $\mu_B^{max}$  value is significantly larger in quantum statistics than in Boltzmann statistics. This feature is also seen in numerical results from the AMPT model [17] and can be understood in terms of the Pauli exclusion principle in quantum statistics. In terms of the thermodynamics relations, this can be understood by examining the first two terms in the Taylor expansion of Eq.(29):

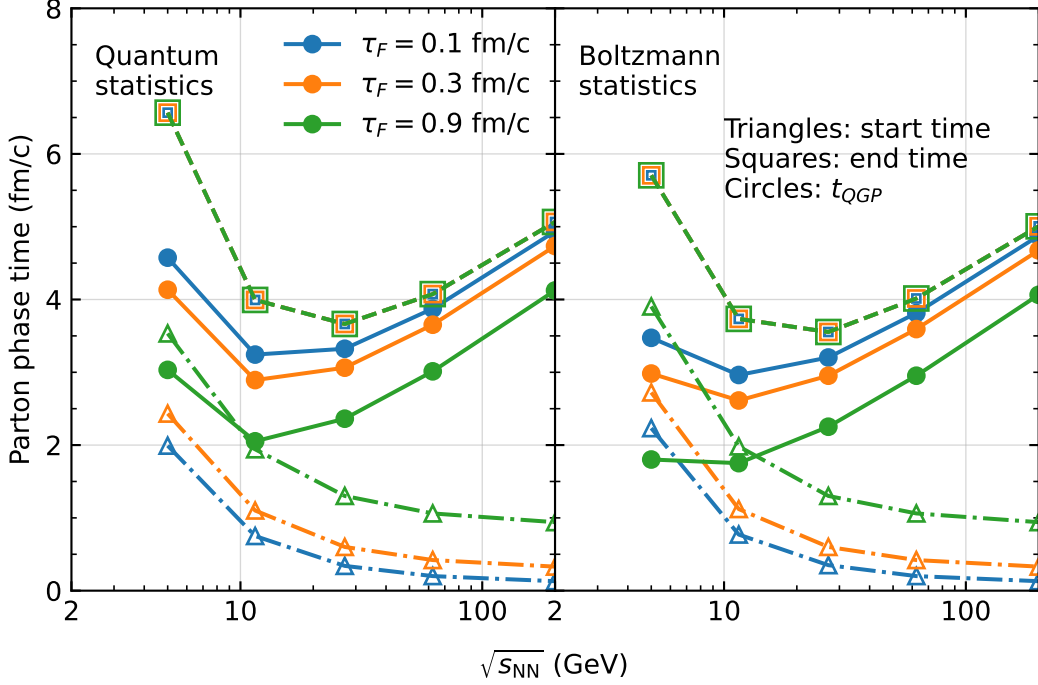


FIG. 8: The start time (triangles), ending time (squares), and lifetime  $t_{QGP}$  (circles) of the QGP phase for  $\tau_F = 0.1$  (blue), 0.3, (orange), 0.9 (green) fm/c for quantum statistics (left panel) and Boltzmann statistics (right panel) as functions of collision energy.

$n_{B,1} \simeq 8\mu_B T^2 / (3\pi^2) + 4\mu_B^3 / (81\pi^2)$ . The coefficient of each term in the above equation is bigger than the corresponding coefficient in Eq.(22) for quantum statistics. As a result, when the same  $n_B$  is used and the  $T$  values are similar for the two statistics,  $\mu_B$  for quantum statistics will be larger.

#### D. QGP lifetime

For each trajectory, we can calculate the time when the system enters the parton phase  $t_{start}$ , the time when it exits the parton phase  $t_{end}$ , and the QGP lifetime spent in the parton phase  $t_{QGP} = t_{end} - t_{start}$ . Specifically, we calculate the first and last times when a  $T - \mu_B$  trajectory intersects the FRG crossover curve [29]. Figure 8 shows these results, where we see that the  $t_{end}$  curves are practically the same for the three formation times used, while  $t_{start}$  increases as  $\tau_F$  increases across all collision energies. As the collision energy increases, we see that the QGP lifetime first decreases until about  $\sqrt{s_{NN}} = 11.5$  GeV before increasing with

$\sqrt{s_{NN}}$ , and this is the case for both statistics. Note that this unexpected non-monotonous dependence of  $t_{QGP}$  on the collision energy has been observed in the numerical results from the AMPT model [17]. For  $\tau_F = 0.1$  or  $0.3$  fm/ $c$ , we see from Fig. 8 that the QGP lifetime at the low energy of  $\sqrt{s_{NN}} = 5$  GeV is still somewhere between 2.6 to 4.6 fm/ $c$ , which indicates a better possibility of studying the QGP properties at lower collision energies than one may naively expect.

#### IV. DISCUSSIONS

Until now, we have considered a QGP consisting of massless quarks and gluons. A more realistic approach would be to consider a massive  $s$ -quark, since  $m_s = 95$  MeV/ $c^2$  [30] is not negligible compared to the system's temperature scale. We have not found an analytical solutions for the total energy density of massive  $s$  and  $\bar{s}$  with quantum statistics; therefore, we create an interpolating function of temperature:

$$\epsilon_s + \epsilon_{\bar{s}} = \frac{6}{\pi^2} \int_0^{\infty} \frac{p^2 \sqrt{p^2 + m_s^2} dp}{e^{\sqrt{p^2 + m_s^2}/T} + 1} = \epsilon_{s+\bar{s}}(T). \quad (34)$$

Note that we have used the relation  $\mu_s = 0$ , which results from  $n_S = n_{\bar{s}} - n_s = 0$  in our semi-analytical model. Considering the finite  $s$ -quark mass, we also obtain the following energy density:

$$\epsilon = \frac{37\pi^2}{30} T^4 + 3 \frac{(\mu_B - 2\mu_S)^2 + \mu_S^2}{2} T^2 + 3 \frac{(\mu_B - 2\mu_S)^4 + \mu_S^4}{4\pi^2} + \epsilon_{s+\bar{s}}(T). \quad (35)$$

The equations for  $n_B$  and  $n_Q$  are unchanged from Eqs.(19) and (20). Therefore, when considering  $m_s \neq 0$  in our model, only the  $\epsilon$  equation changes. We numerically solve these equations using enough  $T$  sampling points for  $\epsilon_{s+\bar{s}}(T)$  to ensure accuracy. In Fig. 9, we compare the resulting  $T - \mu_B$  trajectories to those for  $m_s = 0$  MeV/ $c^2$ . We observe essentially no difference in the  $T - \mu_B$  trajectories when considering a non-zero  $s$ -quark mass. Note that similar lack of effect from finite quark masses have also been seen in numerical studies from the AMPT model [17].

We have observed  $\mu_Q \simeq 0$  in the full solutions for both quantum and Boltzmann statistics, as shown in Figs. 2 and 5. As a result, the partial-1 solution assumes  $\mu_Q = 0$  and then gives almost the same  $T - \mu_B$  trajectories as the full solution. Therefore, a natural question is why  $\mu_Q$  is so small. To answer this question, we first observe that our semi-analytical

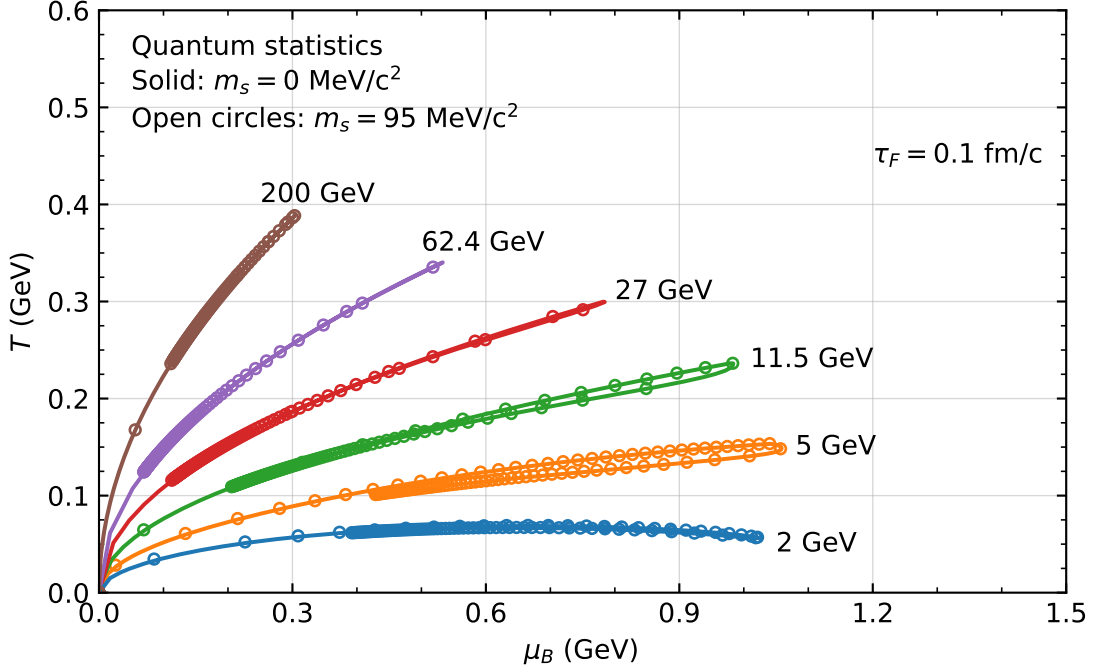


FIG. 9: Trajectories from the full solution for quantum statistics for  $m_s = 0$  (solid) and  $95 \text{ MeV}/c^2$  (open circles) with  $\tau_F = 0.1 \text{ fm}/c$  for central Au+Au collisions at different energies.

model [20] gives  $n_S(t) = 0$ . In addition, our model predicts  $n_Q(t) = n_B(t)/2$  if  $Z = A/2$  for the colliding nuclei. One can verify that,  $n_S = 0$  and  $n_Q = n_B/2$  lead to  $n_Q = 0$  for both statistics. Therefore,  $\mu_Q \simeq 0$  is a consequence of the fact that most nuclei have  $Z \sim A/2$ . Note that recent results from the AMPT model [27] also show  $\mu_Q \approx 0$  [17], although the AMPT model does not assume the  $s$ - $\bar{s}$  symmetry for the initial production and thus does not give  $n_S(t) = 0$ .

Since our model is semi-analytical, it is a convenient tool for calculating the trajectories of nuclear collisions in the QCD phase diagram, either in the conventional  $T - \mu_B$  plane or the more general  $T - \mu_B - \mu_S - \mu_Q$  four-dimensional space. We plan to extend the web interface [31], which currently performs the semi-analytical calculation of  $\epsilon(t)$  for central AA collisions depending on the user input for the colliding system, energy and the proper formation time  $\tau_F$ , to the calculation of  $\epsilon(t)$ ,  $n(t)$ ,  $T(t)$ , and  $\mu(t)$  that have been addressed in this work.

## V. CONCLUSION

We have extended a semi-analytical model, which considers the finite nuclear thickness, to calculate the energy density  $\epsilon(t)$ , net-baryon density  $n_B(t)$ , net-charge density  $n_Q(t)$ , and net-strangeness density  $n_S(t)$  at mid-pseudorapidity averaged over the transverse overlap area in central Au+Au collisions at a range of collision energies. We then extract the temperature  $T(t)$ , net-baryon chemical potential  $\mu_B(t)$ , strangeness chemical potential  $\mu_S(t)$ , and electric charge chemical potential  $\mu_Q(t)$  of the parton system assuming the formation of an equilibrated QGP with either quantum or Boltzmann statistics. The  $n_S(t) = 0$  result from our model for the net-strangeness density leads to  $\mu_B - \mu_Q - 3\mu_S = 0$  for both statistics. We find that the trajectory in the  $T - \mu_B$  plane significantly depends on the statistics; for example, the critical end point from the FRG method is located close to the  $\sqrt{s_{NN}} \sim 4$  GeV trajectory when using quantum statistics but the  $\sqrt{s_{NN}} \sim 3$  GeV trajectory when using Boltzmann statistics. We also find that the  $T - \mu_B$  results from the simpler partial solution that assumes  $\mu_Q = 0$  and  $\mu_S = \mu_B/3$  are very close to the full results, while the results from another partial solution that assumes  $\mu_Q = \mu_S = 0$  significantly underestimate the extracted  $\mu_B$  values.

By calculating the trajectory endpoint as a function of collision energy, we obtain the  $T - \mu_B$  area that the mid-pseudorapidity region of central Au+Au collisions can cover. We find that the accessible area in the phase diagram depends strongly on the parton formation time  $\tau_F$ , once the collision energy is higher than several GeVs. In addition, we have used the Bjorken energy density method, which neglects the finite nuclear thickness, to calculate the energy and net-charge densities. We find that the resulting trajectory starts at higher  $\mu_B$  and  $T$  values than those from our results and later becomes similar to the returning part of our trajectory. When the collision energy is not very high, the peak  $\mu_B$  and  $T$  values are significantly higher than our results, which further demonstrates the importance of including the finite nuclear thickness. While our main results are for a system of massless partons, we have found that using  $m_s = 95$  MeV/ $c^2$  has essentially no effect on the trajectories. Furthermore, we observe an increase in the QGP lifetime as the collision energy decreases below  $\sqrt{s_{NN}} \sim 11.5$  GeV. Overall, this semi-analytical model provides a useful tool for exploring the trajectories of nuclear collisions in the QCD phase diagram in the  $T - \mu_B$  plane or in the more general  $T - \mu_B - \mu_S - \mu_Q$  space.

## Acknowledgments

This work has been partially supported by the National Science Foundation under Grant No. PHY-2012947. We thank Wei-jie Fu, Guo-Liang Ma and Han-Sheng Wang for helpful discussions. We also thank Wei-jie Fu for providing the crossover and CEP results from FRG calculations.

## Appendix: QGP thermodynamics relations between $\epsilon, n$ and $T, \mu$

We consider a quark-gluon plasma composed of gluons  $g$  and three quark flavors  $u, d,$  and  $s$ , similar to a previous study [17]. The total energy, net-baryon, net-electric charge, and net-strangeness densities of such a system are then given by

$$\begin{aligned} \epsilon &= \epsilon_g + \sum_{q=u,d,s} (\epsilon_q + \epsilon_{\bar{q}}), & n_B &= \sum_{q=u,d,s} B_q (n_q - n_{\bar{q}}), \\ n_Q &= \sum_{q=u,d,s} Q_q (n_q - n_{\bar{q}}), & n_S &= \sum_{q=u,d,s} S_q (n_q - n_{\bar{q}}), \end{aligned} \quad (\text{A.1})$$

where  $B_q, Q_q,$  and  $S_q$  are the quark baryon, electric charge, and strangeness numbers, respectively, for quark flavor  $q$ . For parton flavor  $i$ , the energy and number densities are given by

$$\epsilon_i = \frac{1}{2\pi^2} \int_0^\infty dp p^2 \sqrt{p^2 + m_i^2} f_i(p), \quad n_i = \frac{1}{2\pi^2} \int_0^\infty dp p^2 f_i(p), \quad (\text{A.2})$$

respectively, where  $m_i$  represents the parton mass, and  $f_i(p)$  is given by

$$f_i(p) = d_i \left[ \exp \left( \frac{\sqrt{p^2 + m_i^2} - \mu_i}{T} \right) + K \right]^{-1}. \quad (\text{A.3})$$

In the above, the degeneracy factor  $d_i$  is 16 for gluons and 6 for quarks,  $\mu_i$  is the parton chemical potential,  $T$  is the temperature,  $K = 1$  for Fermi-Dirac statistics, and  $K = -1$  for Bose-Einstein statistics. The chemical potential of parton flavor  $i$  is  $\mu_i = B_i \mu_B + Q_i \mu_Q + S_i \mu_S$ , where  $\mu_B, \mu_Q,$  and  $\mu_S$  are the baryon, electric charge, and strangeness chemical potentials, respectively.

## 1. Massless QGP with quantum statistics

For a massless quark-gluon plasma with quantum statistics, we take  $\mu_g = 0$ ,  $\mu_q + \mu_{\bar{q}} = 0$  and then obtain

$$\epsilon_q + \epsilon_{\bar{q}} = -\frac{18T^4}{\pi^2} [Li_4(-e^{-\mu_q/T}) + Li_4(-e^{\mu_q/T})] = \frac{7\pi^2}{20}T^4 + \frac{3\mu_q^2}{2}T^2 + \frac{3\mu_q^4}{4\pi^2}, \quad (\text{A.4})$$

$$n_q - n_{\bar{q}} = \frac{6T^3}{\pi^2} [Li_3(-e^{-\mu_q/T}) - Li_3(-e^{\mu_q/T})] = \mu_q T^2 + \frac{\mu_q^3}{\pi^2}. \quad (\text{A.5})$$

where  $Li_n(z)$  is the polylogarithm function of order  $n$ . Therefore, we obtain the following relations for a massless quark-gluon plasma under quantum statistics:

$$\epsilon = \frac{19\pi^2}{12}T^4 + \frac{(\mu_B + 2\mu_Q)^2 + (\mu_B - \mu_Q)^2 + (\mu_B - \mu_Q - 3\mu_S)^2}{6}T^2 + \frac{(\mu_B + 2\mu_Q)^4 + (\mu_B - \mu_Q)^4 + (\mu_B - \mu_Q - 3\mu_S)^4}{108\pi^2}, \quad (\text{A.6})$$

$$n_B = \frac{\mu_B - \mu_S}{3}T^2 + \frac{(\mu_B + 2\mu_Q)^3 + (\mu_B - \mu_Q)^3 + (\mu_B - \mu_Q - 3\mu_S)^3}{81\pi^2}, \quad (\text{A.7})$$

$$n_Q = \frac{2\mu_Q + \mu_S}{3}T^2 + \frac{2(\mu_B + 2\mu_Q)^3 - (\mu_B - \mu_Q)^3 - (\mu_B - \mu_Q - 3\mu_S)^3}{81\pi^2}, \quad (\text{A.8})$$

$$n_S = -\frac{\mu_B - \mu_Q - 3\mu_S}{3}T^2 - \frac{(\mu_B - \mu_Q - 3\mu_S)^3}{27\pi^2}. \quad (\text{A.9})$$

## 2. Massless QGP with Boltzmann statistics

Using the Maxwell-Boltzmann statistics to describe the thermodynamics of the quark-gluon plasma is equivalent to choosing  $K = 0$  in Eq.(A.3). The general relations between  $\epsilon, n$  and  $T, \mu$  for finite quark masses can be derived [17]. For massless gluons and quarks, we obtain the following simpler equations [17]:

$$\epsilon = \frac{12}{\pi^2}T^4 \left[ 4 + 3 \cosh\left(\frac{\mu_B + 2\mu_Q}{3T}\right) + 3 \cosh\left(\frac{\mu_B - \mu_Q}{3T}\right) + 3 \cosh\left(\frac{\mu_B - \mu_Q - 3\mu_S}{3T}\right) \right], \quad (\text{A.10})$$

$$n_B = \frac{4}{\pi^2}T^3 \left[ \sinh\left(\frac{\mu_B + 2\mu_Q}{3T}\right) + \sinh\left(\frac{\mu_B - \mu_Q}{3T}\right) + \sinh\left(\frac{\mu_B - \mu_Q - 3\mu_S}{3T}\right) \right], \quad (\text{A.11})$$

$$n_Q = \frac{4}{\pi^2}T^3 \left[ 2 \sinh\left(\frac{\mu_B + 2\mu_Q}{3T}\right) - \sinh\left(\frac{\mu_B - \mu_Q}{3T}\right) - \sinh\left(\frac{\mu_B - \mu_Q - 3\mu_S}{3T}\right) \right], \quad (\text{A.12})$$

$$n_S = -\frac{12}{\pi^2}T^3 \sinh\left(\frac{\mu_B - \mu_Q - 3\mu_S}{3T}\right). \quad (\text{A.13})$$

- 
- [1] P. Jacobs and X.-N. Wang, *Prog. Part. Nucl. Phys.* **54**, 443 (2005).
- [2] B. Tomasik and U. A. Wiedemann (2002), hep-ph/0210250.
- [3] J. Adams et al. (STAR), *Nucl. Phys. A* **757**, 102 (2005).
- [4] Y. Aoki, G. Endrodi, Z. Fodor, S. D. Katz, and K. K. Szabo, *Nature* **443**, 675 (2006).
- [5] R. Bellwied, S. Borsanyi, Z. Fodor, J. Günther, S. D. Katz, C. Ratti, and K. K. Szabo, *Phys. Lett. B* **751**, 559 (2015).
- [6] A. Bazavov et al. (HotQCD), *Phys. Lett. B* **795**, 15 (2019).
- [7] R. V. Gavai and S. Gupta, *Phys. Rev. D* **68**, 034506 (2003).
- [8] M. A. Stephanov, *Prog. Theor. Phys. Suppl.* **153**, 139 (2004).
- [9] M. M. Aggarwal et al. (STAR), *Phys. Rev. Lett.* **105**, 022302 (2010).
- [10] J. Adam et al. (STAR), *Phys. Rev. Lett.* **126**, 092301 (2021).
- [11] L. Adamczyk et al. (STAR), *Phys. Rev. Lett.* **112**, 032302 (2014).
- [12] V. Koch, A. Majumder, and J. Randrup, *Phys. Rev. Lett.* **95**, 182301 (2005).
- [13] X. Luo and N. Xu, *Nucl. Sci. Tech.* **28**, 112 (2017).
- [14] B. Zhang, L.-W. Chen, and C. M. Ko, *J. Phys. G* **35**, 065103 (2008).
- [15] Z.-W. Lin, *Phys. Rev. C* **90**, 014904 (2014).
- [16] C. Shen and L. Yan, *Nucl. Sci. Tech.* **31**, 122 (2020).
- [17] H.-S. Wang, G.-L. Ma, Z.-W. Lin, and W.-J. Fu (2021), 2102.06937.
- [18] J. D. Bjorken, *Phys. Rev. D* **27**, 140 (1983).
- [19] Z.-W. Lin, *Phys. Rev. C* **98**, 034908 (2018).
- [20] T. Mendenhall and Z.-W. Lin, *Phys. Rev. C* **103**, 024907 (2021).
- [21] K. Adcox et al. (PHENIX), *Nucl. Phys. A* **757**, 184 (2005).
- [22] S. S. Adler et al. (PHENIX), *Phys. Rev. C* **71**, 034908 (2005).
- [23] J. L. Klay et al. (E895), *Phys. Rev. Lett.* **88**, 102301 (2002).
- [24] J. Barrette et al. (E877), *Phys. Rev. C* **62**, 024901 (2000).
- [25] H. Appelshauser et al. (NA49), *Phys. Rev. Lett.* **82**, 2471 (1999).
- [26] I. G. Bearden et al. (BRAHMS), *Phys. Rev. Lett.* **93**, 102301 (2004).
- [27] Z.-W. Lin, C. M. Ko, B.-A. Li, B. Zhang, and S. Pal, *Phys. Rev. C* **72**, 064901 (2005).
- [28] A. Monnai, B. Schenke, and C. Shen, *Int. J. Mod. Phys. A* **36**, 2130007 (2021).



- [29] W.-J. Fu, J. M. Pawlowski, and F. Rennecke, Phys. Rev. D **101**, 054032 (2020).
- [30] P. A. Zyla et al. (Particle Data Group), PTEP **2020**, 083C01 (2020).
- [31] A web interface that calculates the average initial energy density at mid-pseudorapidity of central A+A collisions with the semi-analytical method of Ref. [20] is available at <http://myweb.ecu.edu/linz/densities/> (2021).